Journal of Alloys and Compounds 744 (2018) 778–784

Contents lists available at ScienceDirect

Journal of Alloys and Compounds

journal homepage: http://www.elsevier.com/locate/jalcom

Effects of Y on helium behavior in Y-doped TiH_2 films prepared by magnetron sputtering

Zhibin Han [a, b], Chunjie Wang [a, b], Guijun Cheng [a, b], Hongliang Zhang [a, b], Ranran Su [a, b], Yiming Duan [a, b], Jie Gao [c], Xiaojie Ni [d], Bangjiao Ye [d], Wei Zhang [a, b], Liqun Shi [a, b, *]

[a] Applied Ion Beam Physics Laboratory, Institute of Modern Physics, Fudan University, Shanghai 200433, PR China
[b] Department of Nuclear Science and Technology, Fudan University, Shanghai 200433, PR China
[c] Chinese Acad Sci, Shanghai Inst Appl Phys, Shanghai 201800, PR China
[d] State Key Laboratory of Particle Detection and Electronics, University of Science and Technology of China, Hefei 230026, PR China

ARTICLE INFO

Article history:
Received 30 July 2017
Received in revised form
1 February 2018
Accepted 2 February 2018
Available online 6 February 2018

Keywords:
Helium behaviors
Hydrogen storage
Yttrium-doped
Magnetron sputtering

ABSTRACT

TiH_2 and yttrium-doped TiH_2 alloy films with different helium concentrations prepared by magnetron sputtering were investigated using ion beam analysis (IBA), X-ray diffraction (XRD), thermal helium desorption spectrometry (THDS), positron annihilation spectroscopy (PAS) and nanoindentation techniques. It was found that through increasing the concentration of doped Y atoms, strong release peaks of helium will be found at about 820 K. The release at 820 K corresponds to the binding energy of the helium state on grain boundary indicating that the majority of the helium exists in the grain boundaries. In addition, the results of XRD and nanoindentation indicate that the doping of Y in the TiH_2 films can improve the hardness and the elastic modulus of the films because of the fine-grain strengthening caused by the decreased size of TiH_2 grains.

1. Introduction

Tritium, an important hydrogen isotope, is a key component of future fusion energy production [1]. However considering its radioactivity and high diffusion coefficient in materials, the storage of the tritium is a key problem in the nuclear technology. Compared to traditional liquefied gas, storing tritium as tritide always attracts scientists' attention because of its higher safety and lower cost. Titanium tritide is recommended for its properties of low level of radioactivity, low equilibrium pressure, low cost, greater stability to air and high tritium capacity than other metal tritides such as La-Ni-Al alloys and zirconium [2]. The tritium nucleus decays by low energy (<18.59 keV) beta emission to helium-3 ($T \rightarrow {}^3He + \beta + \nu$) with a half-life period of 12.3 years. The resultant helium atoms (inert gas) have a strong tendency to aggregate into bubbles because of their insolubility and high mobility in tritide [3]. The evolution of the helium bubbles leads to swelling, flaking and blistering in a material which is associated with helium embrittlement [4,5]. Hence, the life time of the tritide for use is directly determined by the consequence of the helium inclusions which is a function of the concentration of tritium in the original material.

To reduce the impact of incorporated He in titanium tritide, some alloys like Ti-Y, Ti-Zr, Ti-Mo have been investigated [6,7]. Ti-Y alloy has some favorable properties such as thermal, stability and ductility compared to pure Ti [7]. Ti-Y alloy films also show better performance in helium induced embrittlement [8]. Jinchao Zhang and coworkers proved that the Y atoms in the alloy will dissolve out as Y_2O_3 nanoparticles and nanorods along the (002) plane at room temperature. In our previous study, the Y atoms dissolved into the titanium hydride uniformly with the introduction of hydrogen at room temperature [9]. However, the crystal structures in the Ti-Y system and Ti-Y-H system are different. Therefore, the research on helium induced properties of the yttrium-doped titanium hydride warrants intense study.

In this paper, we report the effect of the doped yttrium atoms on helium behavior in TiH_2 films with different helium concentration prepared by magnetron sputtering on a Si (100) substrate. In the thermal helium desorption experiments, it was found there was a strong release feature at about 820 K with increasing concentration of doped Y atoms. This desorption temperature of helium at 820 K corresponds to the helium state in the grain boundary, indicating that helium atoms with a significant concentration were captured

---

* Corresponding author. No. 220 Handan Road, Shanghai 200433, PR China. Tel.: +86 2165642292; fax: +86 21 65642782.
E-mail address: lqshi@fudan.edu.cn (L. Shi).

https://doi.org/10.1016/j.jallcom.2018.02.022

in the grain boundary. It suggested that the doped Y atoms impacted on either the creation of more grain boundaries or the capture of more He in the grain boundaries. It should be noted that we employed hydrogen and He^4 instead of tritium and He^3 in our work considering the radiation hazard of tritium and the similarity of the properties to protons and He^4 by nature of their same electric structure. Their difference in mass will only have a secondary effect in this situation.

2. Experiment

2.1. Specimens preparation

The TiH_2 and Y-doped TiH_2 films with different helium concentrations were deposited on molybdenum and silicon substrates by using DC magnetron sputtering. The substances were cleaned ultrasonically before use. A pure titanium target (99.99%), on which pure yttrium (99.99%) pieces were distributed evenly, was used for sputtering and this target was placed on a water cooled cathode during the sputtering. The doping of yttrium was controlled by altering the quantity of the yttrium pieces on the titanium target during the deposition. The base pressure of the chamber before sputtering was less than 1×10^{-5} Pa. The sputtering atmosphere used in the deposition was a mixture of 99.99% pure hydrogen, 99.99% helium and 99.995% argon. To obtain different concentrations of helium in the Y-doped TiH_2 films, the proportion of hydrogen, helium and argon in the mixture was controlled by three mass flowmeters. The proportion of hydrogen, helium and argon (Q_H /Q_{He} /Q_{Ar}) was 2:6.5:2, 2:12:2 and 2:19:2 (The unit is Standard Cubic Centimeter per Minute). The deposition temperature of the samples was around the room temperature during the whole deposition process. The sputtering pressure and power were 1.1 Pa and 92.4 W respectively and all films were deposited for 1.5 h with a bias voltage of 65 V [10].

2.2. Characterization

Ion beam analysis (IBA) with elastic recoil detection analysis (ERDA) was employed to determine the hydrogen and helium concentrations at the NEC 95DH-2 × 3 MeV pelletron tandem accelerator of Fudan University. During the whole measurement, Au/Si surface barrier detectors were fixed at the laboratory angles of 165° and 30° respectively relative to the incident beam and the background pressure of the chamber was less than 5×10^{-5} Pa. The solid angles of the RBS and ERD detector were 1.83×10^{-3} sr and 1.12×10^{-3} sr respectively. The depth profiles of the light elements (hydrogen and helium) were measured simultaneously by using 8.5 MeV carbon ions [11]. In the ERD analysis, the samples were tilted by 70° to the sample normal and a 10 μm thick Mylar foil was set in front of the ERD detector to absorb the scatted carbon ions. The hydrogen and helium atomic concentration ([H or He]/[Ti] × 100 at.%) distributions were derived from the ERD spectra by Alegria 1.2 code [12]. The thickness and yttrium component of the films, measured by RBS with 3.8 MeV helium ions beam, were calculated by SIMNRA 6.03 program [13]. The incident helium ion beam was normal to the sample surface.

The crystal structure of the samples was characterized by X-ray diffraction (XRD) at a D8 ADVANCE and DAVINCI. DESIGN X-ray diffractometer made by Bruker, Germany. The diffractometer was used in a two theta mode from 10° to 68° with 0.02° per step using a Cu Kα source. The thermal helium desorption spectrometry (THDS) was used for the investigation of the interaction between helium and the defects in materials, based on the determination of the release rate of helium in the sample by measuring its partial pressure during heating with a linear temperature ramp. The thermal desorption profile was measured with a Quadrupole Mass Spectrometer (QMS) as the samples mounted in a molybdenum crucible were resistance heated using a linear temperature ramp from room temperature to 1773 K (1500 °C) at a rate of 1 K/s.

The defect profiles in the samples were characterized by positron annihilation spectroscopy (PAS) at State Key Laboratory of Particle Detection and Electronics, University of Science and Technology of China. Positrons are easily trapped by vacancy defects, resulting in a narrowing of 511 keV annihilation peak compared to bulk annihilation. The S parameter was defined as a fraction of counts in the central region of the annihilation peak. The mechanical properties (hardness and elastic modulus) of the films were characterized using the nanoindenter G200 from the Agilent corporation (America) in the continuous stiffness measurement (CSM) mode, whose maximum load is 500 mN. The indenter was equipped with a diamond Berkovich indenter (triangular based pyramid) and was calibrated by the classical method consisting of indenting a fused silica sample at different loads.

3. Result and discussion

3.1. Structural characterization of Y-doped TiH_2 films

The Y doped TiH_2 films on a Si substrate were analyzed with a 3.8 MeV He ion beam scattered into a detector at 165° (Fig. 1). The doping concentration of yttrium and the thickness of the films were determined by fitting the RBS spectra with SIMNRA. The concentrations of yttrium ([Y]/([Y]+[Ti]) × 100 at.%) were determined to be 5% and 8%, which were hereafter denoted as 5%Y films and 8%Y films respectively. The thickness of the films was approximately 1.2 μm. The H to Ti ratio was 1.7:1, which suggests that the Ti mainly existed as a TiH_2 phase in the films, as confirmed in the XRD analyses. Y-doped TiH_2 films with different helium concentration of approximately 3 at.%, 7 at.% and 14 at.% ([He]: [Ti] × 100 at.%) were prepared by controlling the relative helium flow rate (Q_{He} /Q_{Ar} = 6.5:2, 12:2 and 19:2) [14] and the results of the corresponding He depth profiles are shown in Fig. 2.

The XRD patterns of Y-doped TiH_2 films deposited on Si substrates with different helium concentration are shown in Figs. 3–5 respectively. The Si substrates were single crystal Si (100) and only the Si (400) peak appeared at 2θ = 69.17°, hence there was no Si peak in all the XRD patterns of the films from 10° to 68°. In Figs. 3–5, the patterns of the Y-doped TiH_2 films exhibited two

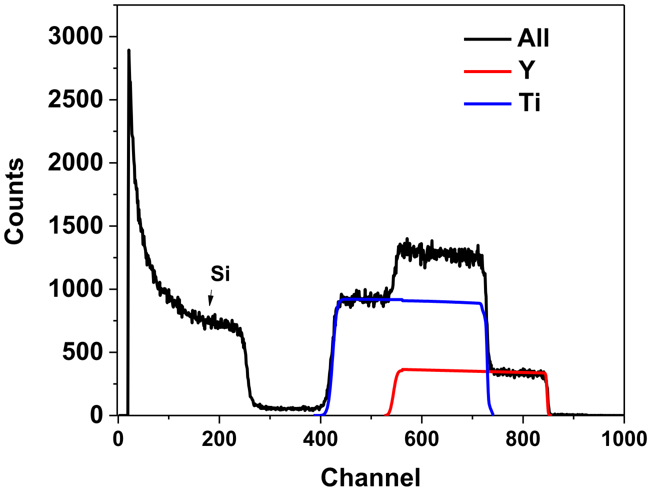

Fig. 1. The RBS spectra of Ti+8%Y film deposited on Si substrate using 3.8 MeV ^{4}He ion beam. The scattering angle is 165°.

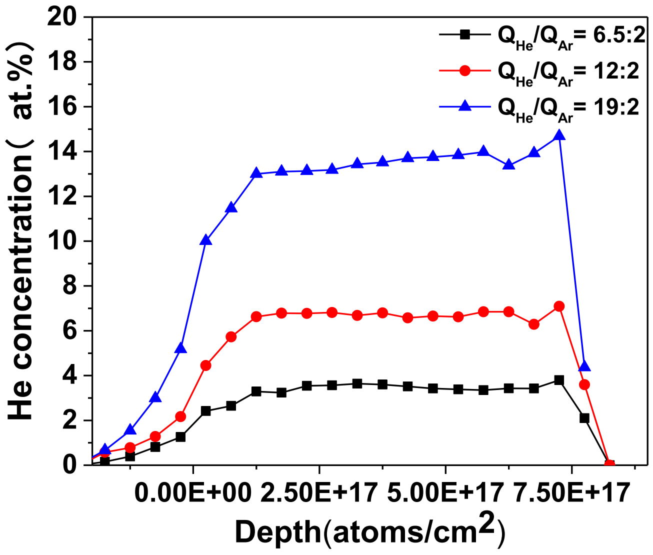

Fig. 2. Helium depth profiles of 8%Y doped TiH_2 films deposited on Si substrates at 1.1 Pa with different relative helium flow rate Q_{He}/Q_{Ar}.

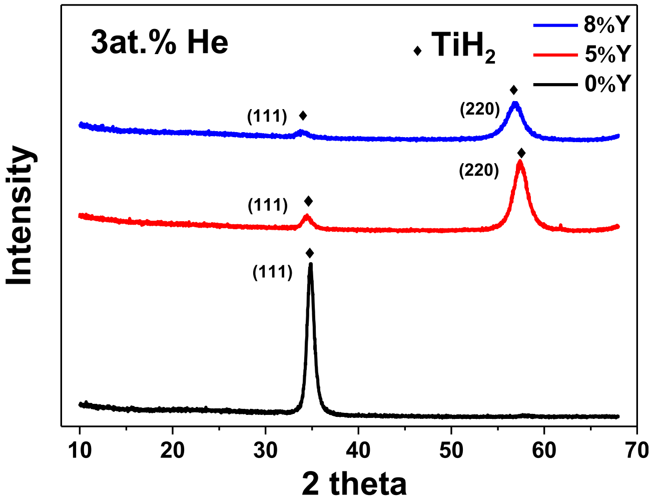

Fig. 3. XRD patterns of TiH_2 and yttrium-doped TiH_2 alloy films with about 3 at.% helium deposited on Si substrates at 1.1 Pa.

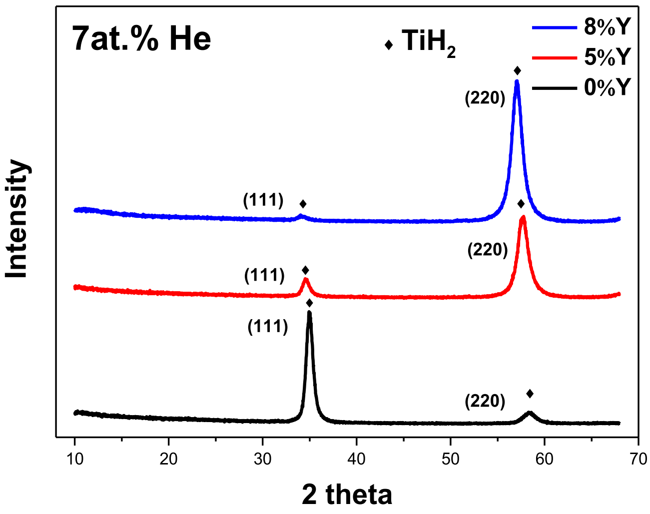

Fig. 4. XRD patterns of TiH_2 and yttrium-doped TiH_2 alloy films with about 7 at.% helium deposited on Si substrates at 1.1 Pa.

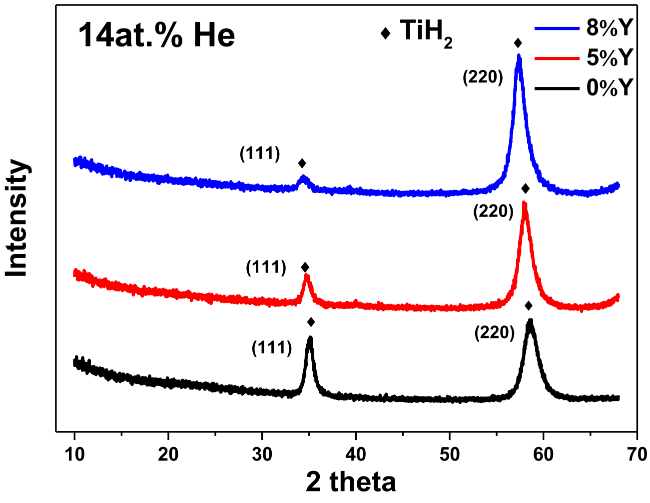

Fig. 5. XRD patterns of TiH_2 and yttrium-doped TiH_2 alloy films with about 14 at.% helium deposited on Si substrates at 1.1 Pa.

peaks (111) and (220) at $2\theta = 34.75°$ and $2\theta = 58.08°$ respectively [15], both of which indicate that the alloy films exist as the fcc (face-centered cubic) TiH_2 phase. Though the Y atoms were mixed into the films, there were no extra phase of yttric compound in the patterns. However, with the increase of the Y atoms, a significant peak shift of the Y-doped TiH_2 films was observed in Figs. 3–5. Corresponding Δd /d is 0.02 when the concentration of Y increases to 8% from 0%. This lattice increase can be attributed to the lattice expansion caused by the dissolution of Y atoms in the TiH_2 [9]. In Fig. 3, with no doping of yttrium, the (111) surface has the lowest surface energy in all the (hkl) planes, exhibiting a distinct preferred orientation [16]. With the increase of the doped Y atoms, the diffraction peaks become boarder and the main peak gradually changes to the (220) and the preferred orientation of (111) disappears. As is in our previous work [9], some of the Y atoms preferentially combined with the oxygen contamination remaining in the plasma and formed tiny disordered Y_2O_3 nanoclusters dispersing in the TiH_2; the others existed as YH_2 in the TiH_2 films. In thermodynamic theory, the structure of crystallization is made up of three contributions during grains growth process: the bulk strain energy, the energy of the top-most surface and the energy contribution from other interfaces such as the substrate interface [17]. Due to the strain caused by the yttric compound, a change of preferred orientation has occurred with the increase of yttric doping. In Figs. 3–5, by comparing the patterns of Y-doped TiH_2 films with the different helium concentration, we can find that the increase of helium concentration has also weakened the diffraction peak. This effect will be discussed further below.

3.2. Thermal desorption experiments

The thermal desorption result of Y-doped TiH_2 alloy films with different helium concentrations (Figs. 6–8) allows the determination of defect binding energy of the He. The model of Redhead [18] which is based on the first-order desorption mechanisms can be used to simulate the helium desorption states, and the desorption rate L(t) is given by Eq. (1).

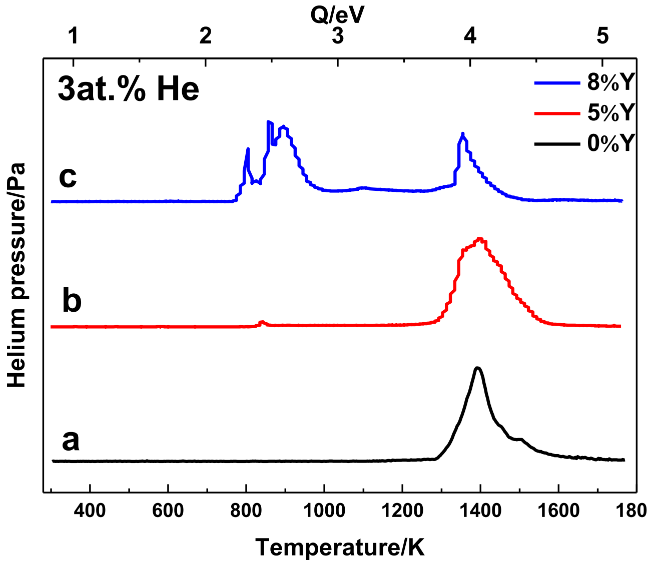

Fig. 6. Thermal desorption spectra of TiH_2 and yttrium-doped TiH_2 alloy films with about 3 at.% helium deposited on Mo substrates at 1.1 Pa.

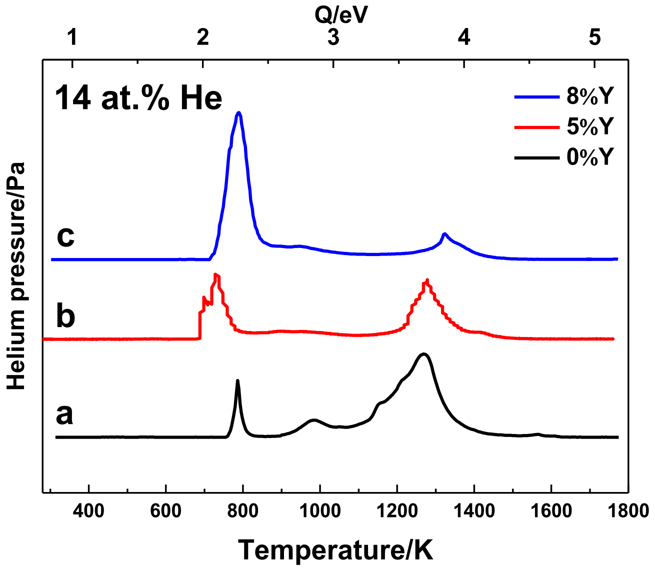

Fig. 8. Thermal desorption spectra of TiH_2 and yttrium-doped TiH_2 alloy films with about 14 at.% helium deposited on Mo substrates at 1.1 Pa.

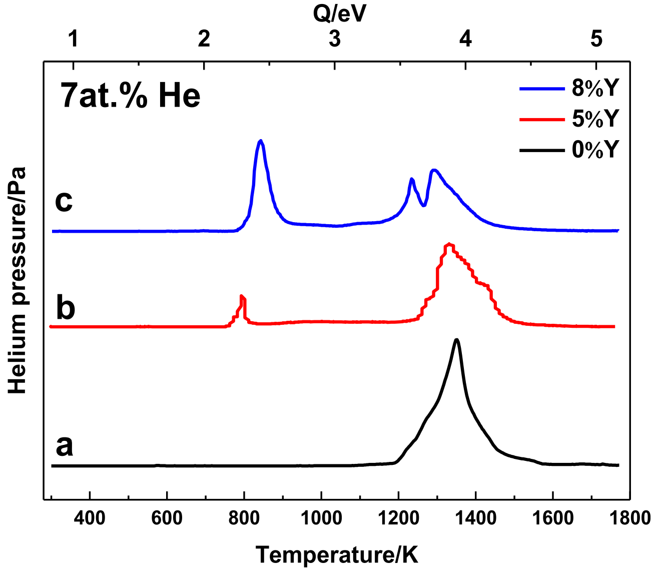

Fig. 7. Thermal desorption spectra of TiH_2 and yttrium-doped TiH_2 alloy films with about 7 at.% helium deposited on Mo substrates at 1.1 Pa.

$$L(t) = \frac{dN}{dt} = -\mathrm{N}\nu\exp\left(-\frac{\mathrm{E}}{\mathrm{kT}}\right). \tag{1}$$

where N is the number of the desorption atoms from the sample, ν is the attempt frequency of the atoms in the grains ($\nu \approx 10^{13}$/s), E is the dissociation activation enthalpy, k is the Boltzmann constant, and T is the absolute temperature, assuming a linear heating, $T = T_0 + \beta t$ in which T_0 is the initial temperature, β is the ramp rate, and t is the heating time. From Eq. (1), we can acquire the relationship between the temperatures of maximum desorption and the He binding energy.

$$\frac{E}{KT^2} = \frac{\upsilon}{\beta}\exp\left(-\frac{E}{KT}\right). \tag{2}$$

Based on Eq. (2), the helium dissociation energy that corresponds to the desorption peaks was on top of the coordinate axis, as are shown in Figs. 6–8. In this study, all the helium desorption curves can be divided into three main zones to represent three kinds of helium bounding state, to be specific, zone I, II, and III represent the temperatures less than 650 K, around 820 K (from 650 to 1100 K) and 1350 K (higher than 1100 K) respectively.

3.3. Discussion

In the thermal helium desorption experiments, the dissociation activation energies of different helium states are different, in which mobile helium, helium clusters, and different sizes of helium bubbles in different lattice position of the grains are included. Below 650 K (zone I), there is no obvious release peak and the proportion of helium release (Figs. 6–8) is very small (less than 0.1%). By referring to previous experimental and simulation results [19–21], for the dissociation energies of 1.2–2.0eV, it can be concluded that the degassing helium atoms are probably interstitial helium atoms or single helium atoms with low binding energies that escaped from the interstitial helium precipitates in the grains. The dissociation energies of helium atoms in Zone II and Zone III are equal to 2.3eV and 3.8 eV which correspond to the helium state in grain boundaries and helium bubbles in the interior of the grain respectively.

During the thermal desorption, almost all the hydrogen atoms are released at 650 K (Fig. 9), which coincides with a phase transformation of Ti-H that occurs at this temperature according to the phase diagram of titanium hydride [22]. Though a large number of hydrogen atoms are released, nearly no helium is released in this diffusion and reconstruction processes during the transformation of TiH_2 to Ti. By comparing Figs. 6a–8a, the thermal desorption spectra of TiH_2 only reveals obvious helium release peaks in Zone III (around 1350 K) where the helium concentration is 3 at.% and 7 at.% respectively. For the helium concentration of 14 at.% in the films, helium atoms started to release in Zone II (around 820 K). The phenomenon in Fig. 8a indicates the evolution of helium atoms in materials. During the starting deposition of the films in the plasma, helium atoms backscattered from the titanium target were implanted evenly into the alloy through magnetron sputtering.

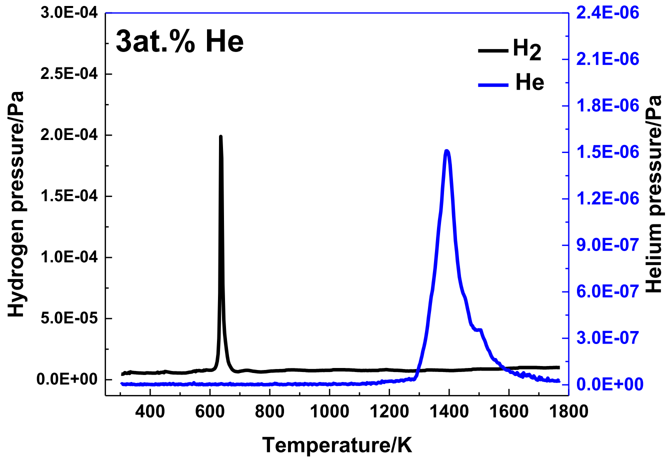

Fig. 9. Thermal desorption spectra for H_2 and He from the titanium hydride sample with 3 at.% ([He]/[Ti]).

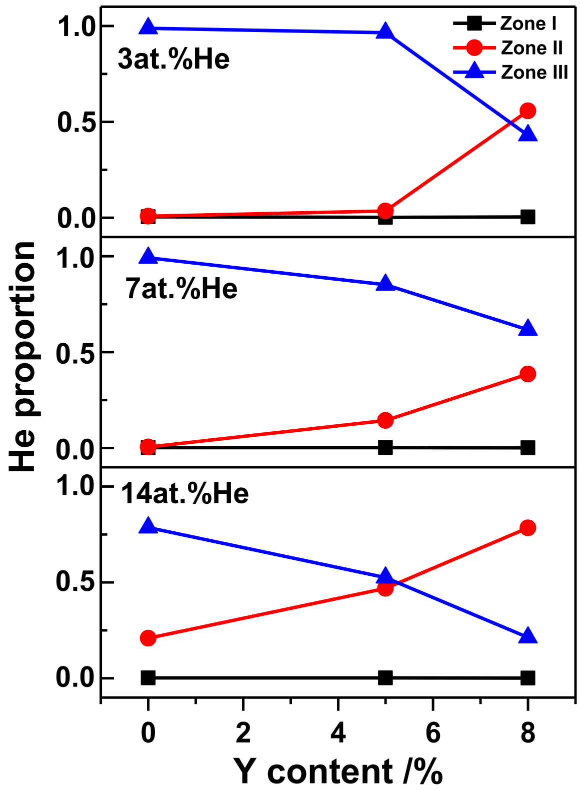

Fig. 10. The helium proportion in each desorption zones in the TiH_2, 5%Y and 8%Y doped TiH_2 films with different helium concentration.

Then helium atoms will preferentially combine with the defects in film and become helium vacancy complexes (He_nV_m) [23]. With a low activation diffusion energy (about 0.4eV) [24], interstitial helium atoms will migrate to the helium vacancy complexes or act as sinks for nearby self-interstitials (SIAs) [25]. After the accumulation of helium atoms, He bubbles of different sizes will be distributed throughout the lattice. Further growth of helium bubbles will occur through migration and consolidation mechanism or Ostwald ripening mechanism [26]. In zone III, the release of helium atoms from helium bubbles of different sizes takes place with relative higher binding energy than in zone II [21]. By comparing zone III in Figs. 6a–8a, the helium desorption peaks of helium bubbles move to lower temperature gradually with the increase of helium concentration: the main peaks at 1397 K (3 at.% of helium), 1351 K (7 at.%) and 1271 K (14 at.%) correspond to the dissociation energies of 4.05 eV, 3.91eV and 3.67 eV, respectively. And there is a knee peak in higher temperature (about 1500 K) in Fig. 6a when the helium concentration is 3 at.%. According to the experiment and calculation results of helium bubbles [21,27], the higher the desorption temperature is, the smaller size the helium bubble is. It indicated that nearly all the helium bubbles in the TiH_2 exist in different sizes and shapes and the size of helium bubbles will become larger with the accumulation of helium atoms in TiH_2. The phenomenon that the lattice distortion is caused by these high-pressure helium bubbles in the grains is consistent with the above XRD results in Figs. 3–5 [10]. In Fig. 8a, the helium release in zone II can be considered to come from the helium in grain boundaries. According to experiment results in aged TiT_2 [21], the deterioration of the lattice leads to the grain refining, hence, more grain boundaries formed in the films will increase qualities of helium bubbles in boundaries. In addition, the dissociation energy of helium bubbles from grain boundaries is quite lower than those in the interior of the TIH_2 grain. In zone II, helium bubbles in the grain boundaries will connect with each other to form networks in the films, and those networks will become an easy path for the helium atoms to percolate to the surface [28].

Fig. 10 shows the helium proportion in each desorption zones in the TiH_2, TiH_2 with 5%Y and TiH_2 with 8%Y films with different helium concentration. The helium release increases significantly in zone II with the increase of doped Y atoms for all helium concentrations. By comparing the XRD results in Figs. 3–5, these extra grain boundaries forming in the films were due to the grain refinement caused by the doping of yttrium atoms in the grains. When the yttrium concentration increases from 0% to 8% as is shown in Fig. 10, the helium release peaks increase greatly in zone II, nearly 80% of helium atoms were released in zone II when the doping of Y was 8% (Figs. 8c and 10). In the thermal desorption spectrum (shown in top axis of Figs. 6–8), the corresponding binding energy of helium atoms in zone II and zone III, is about 2.3 eV and 3.8 eV respectively, which is calculated by Equation (2). Through comparing the binding energy of helium atoms in tritide [19,21], the helium release in zone II corresponds to the grain boundaries state, while desorbing helium atoms from the helium bubbles in the interior of the grain needs a higher energy. This indicates that most of the helium atoms exist in the grain boundaries under these conditions. In Fig. 8, the helium release peaks in zone III move gradually towards a higher temperature with the increase of doped Y, indicating that the helium bubbles have a smaller size inside the grains because they have diffused to the grain boundary.

The depth profiles of defects in Y-doped TiH_2 films were measured using a mono-energetic positron beam with the energy from 0.5 keV to 20 keV. For Y-doped TiH_2 films with different helium concentrations and yttrium content, the S-parameter as a function of positron implantation energy is shown in Figs. 11 and 12. In Fig. 11, with the increase of helium concentration, the S-parameters in the films increase rapidly indicating that the increased helium concentration creates more defects in the TiH_2 grains. There was no major change of S-parameters for the Y-doped TiH_2 films when increasing the concentration of doped Y (Fig. 10) though it does increase slightly for 8% Y. This indicates the lattice defects were mainly caused by the helium bubbles in the Y-doped TiH_2 films [29].

In order to investigate the effect on mechanical properties caused by the doping of yttrium atoms in the films, the results of hardness and elastic modulus test were provided in Fig. 13. The

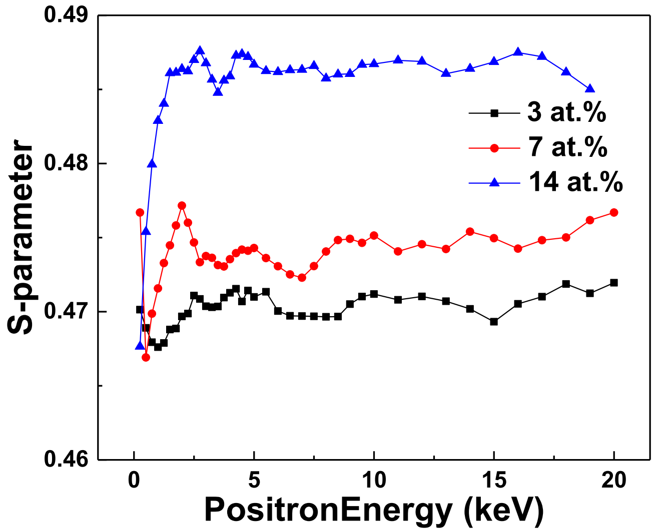

Fig. 11. The S-parameter as a function of positron implantation energy for 5%Y doped TiH_2 films with different helium concentration.

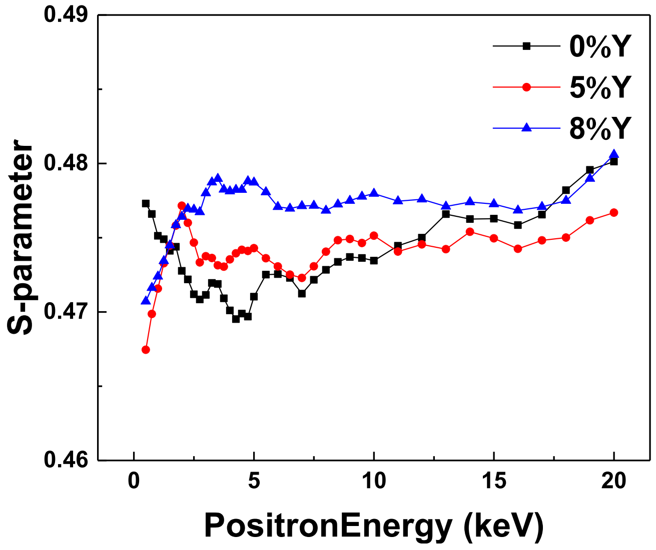

Fig. 12. The S-parameter as a function of positron implantation energy for Y-doped TiH_2 films with different doping content of yttrium and 7 at.% of helium.

hardness values of the 5%Y film and the 8%Y film under the same helium and hydrogen concentration have a remarkable increase of 10% and 30%, respectively. A similar increase is also found for the elastic modulus of these films. The same phenomenon was also found by Zhang et al.' [8]. With the doping of yttrium atoms in the titanium films, mechanical properties are enhanced significantly and this increase has been attributed to the effects of the doped Y in the TiH_2 films: fine-grain strengthening was caused by decreased size of TiH_2 grains [8].

4. Conclusions

The influence of alloying on bubble evolution and helium release process in magnetron sputtered Y-doped TiH_2 alloy films with different helium concentration has been studied by IBA, XRD, TDS and PAS. The corresponding mechanical properties of the alloy films were examined by the nanoindentation technique. In the

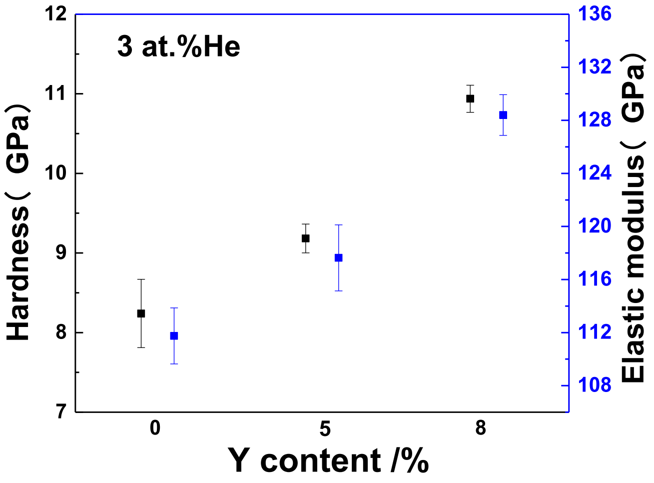

Fig. 13. The hardness and elastic modulus of helium-containing TiH_2 and Y-doped TiH_2 films with a thickness of about 1.2 μm on Si substances with about 3 at.% helium deposited under $Q_{He}/Q_{Ar} = 6.5$: 2.

thermal desorption experiments, as the concentration of Y atoms increases, major release peaks appear at about 820 K and nearly 80% of helium atoms are released in zone II when the doping of Y was up to 8%. It suggested that this release peak corresponds to the helium bubbles in the grain boundary. And these new grain boundaries were created by the decreased size of TiH_2 grains with the doping of Y atoms. In addition, the nanoindentation results indicate that the doping of Y in the TiH_2 films can improve the hardness and the elastic modulus of the films because of the fine-grain strengthening caused by the decreased size of TiH_2 grains.

Acknowledgments

The authors are grateful to the staff of the tandem accelerator in The Key Lab of Applied Ion Beam Physics at Fudan University, for their cooperation during the ion beam analysis experiments. Our work was supported by the National Nature Science Foundation of China under Grant No. 11375046.

References

[1] R. Smith, D.A.J. Whittaker, B. Butler, A. Hollingsworth, R.E. Lawless, X. Lefebvre, S.A. Medley, A.I. Parracho, B. Wakeling, Hydrogen isotope separation for fusion power applications, J. Alloy Comp. 645 (2015) S51–S55.

[2] L.E. Klebanoff, J.O. Keller, 5 years of hydrogen storage research in the U.S. DOE Metal Hydride Center of Excellence (MHCoE) (vol 38, pg 4533, 2013), Int. J. Hydrogen Energy 38 (2013), 8022–8022.

[3] L. Liang, M. Ma, W. Xiang, Y. Wang, Y. Cheng, X. Tan, A molecular dynamics simulation study of temperature and depth effect on helium bubble releasing from Ti surface, J. Alloy Comp. 645 (2015) S166–S169.

[4] X.S. Zhou, Q. Liu, L. Zhang, S.M. Peng, X.G. Long, W. Ding, G.J. Cheng, W.D. Wang, J.H. Liang, Y.Q. Fu, Effects of tritium content on lattice parameter, 3He retention, and structural evolution during aging of titanium tritide, Int. J. Hydrogen Energy 39 (2014) 20062–20071.

[5] C.L. Chen, A. Richter, R. Kögler, The effect of dual Fe+/He+ ion beam irradiation on microstructural changes in FeCrAl ODS alloys, J. Alloy Comp. 586 (2014) S173–S179.

[6] B.L. Liu, S. Liu, L.B. Wang, Investigation on helium bubbles shape in Ti and Ti alloy by transmission electron microscopy, Atomic Energy Sci. Technol. 42 (2008) 799–803.

[7] E.T. Zhao, Y.Y. Chen, F.T. Kong, C.J. Zhang, S.L. Xiao, Effect of yttrium on microstructure and mold filling capacity of a near-alpha high temperature titanium alloy, China Foundry 9 (2012) 344–348.

[8] J.C. Zhang, E.D. Wu, S. Liu, Effects of Y on helium behavior in Ti-Y alloy films, J. Nucl. Mater. 454 (2014) 119–125.

[9] Z.B. Han, G.J. Cheng, L.Q. Shi, Synthesis and characterization of Y-doped TiH2 films prepared by magnetron sputtering, Int. J. Hydrogen Energy 41 (2016) 2820–2828.

[10] L.Q. Shi, C.Z. Liu, S.L. Xu, Z.Y. Zhou, Helium-charged titanium films deposited

by direct current magnetron sputtering, Thin Solid Films 479 (2005) 52–58.

[11] E. Markina, M. Mayer, H.T. Lee, Measurement of He and H depth profiles in tungsten using ERDA with medium heavy ion beams, Nucl. Instrum. Methods Phys. Res. Sect. B Beam Interact. Mater. Atoms 269 (2011) 3094–3097.

[12] F. Schiettekatte, A. Chevarier, N. Chevarier, A. Plantier, G.G. Ross, Quantitative depth profiling of light elements by means of the ERD ExB technique, Nucl. Instrum. Methods Phys. Res. Sect. B Beam Interact. Mater. Atoms 118 (1996) 307–311.

[13] M. Mayer, SIMNRA, Max-Planck-Institut für Plasmaphysik, Garching, Version 6.03.

[14] Z.B. Han, C.J. Wang, L.Q. Shi, Synthesis and characterization of helium-charged titanium hydride films deposited by direct current magnetron sputtering with mixed gas, Mater. Des. 119 (2017) 180–187.

[15] JCPDS, 25-0984.

[16] C. Liu, N. Jin, Z. Li, X. Liu, First-principles calculations on the electronic structure and bonding nature of TaN(111)/TiN(111) interface, J. Alloy Comp. 717 (2017) 326–332.

[17] D.R. McKenzie, M.M.M. Bilek, Thermodynamic theory for preferred orientation in materials prepared by energetic condensation, Thin Solid Films 382 (2001) 280–287.

[18] P.A. Redhead, Thermal desorption of gases, Vacuum 12 (1962) 203–211.

[19] E. Oliviero, M.F. Beaufort, J.F. Barbot, A. van Veen, A.V. Fedorov, Helium implantation defects in SiC: a thermal helium desorption spectrometry investigation, J. Appl. Phys. 93 (2003) 231–238.

[20] T. Schober, H. Trinkaus, He-3 bubble formation in titanium tritides at elevated-temperatures - a tem study, Philos. Mag. A-Phys. Condens. Matter Struct. Defect Mech. Prop. 65 (1992) 1235–1247.

[21] G.J. Cheng, L.Q. Shi, X.S. Zhou, J.H. Liang, W.D. Wang, X.G. Long, B.F. Yang, S.M. Peng, Thermal desorption behavior of helium in aged titanium tritide films, J. Nucl. Mater. 466 (2015) 615–620.

[22] Asm, Alloy phase diagrams. Asm handbook, in: ASM International, vol. 3, 1992.

[23] P.N. Ma, L. Pollet, M. Troyer, F.C. Zhang, A classical picture of the role of vacancies and interstitials in Helium-4, J. Low Temp. Phys. 152 (2008) 156–163.

[24] Y.F. Lu, L.Q. Shi, W. Ding, X.G. Long, First-Principles study of hydrogen impact on the formation and migration of helium interstitial defects in hcp titanium, Chin. Phys. Lett. 29 (2012) 013102.

[25] T. Seletskaia, Y.N. Osetsky, R.E. Stoller, G.M. Stocks, Calculation of helium defect clustering properties in iron using a multi-scale approach, J. Nucl. Mater. 351 (2006) 109–118.

[26] J. Gao, L.M. Bao, H.F. Huang, Y. Li, J.R. Zeng, Z. Liu, R.D. Liu, L.Q. Shi, Evolution law of helium bubbles in hastelloy N alloy on post-irradiation annealing conditions, Materials 9 (2016) 5.

[27] J. Wang, Q. Hou, Molecular dynamics simulation of helium cluster growth in titanium, Acta Phys. Sin. 58 (2009) 6408–6412.

[28] C.S. Snow, J.F. Browning, G.M. Bond, M.A. Rodriguez, J.A. Knapp, He-3 bubble evolution in ErT2: a survey of experimental results, J. Nucl. Mater. 453 (2014) 296–306.

[29] R.S. Brusa, G.P. Karwasz, N. Tiengo, A. Zecca, F. Corni, R. Tonini, G. Ottaviani, Formation of vacancy clusters and cavities in He-implanted silicon studied by slow-positron annihilation spectroscopy, Phys. Rev. B 61 (2000) 10154–10166.